UC Berkeley
UC Berkeley Previously Published Works

Title

Emergence of the Vortex State in Confined Ferroelectric Heterostructures

Permalink

https://escholarship.org/uc/item/450930r4

Journal

Advanced Materials, 31(36)

ISSN

0935-9648

Authors

Hsu, Shang-Lin
McCarter, Margaret R
Dai, Cheng
et al.

Publication Date

2019-09-01

DOI

10.1002/adma.201901014

Peer reviewed

Emergence of the Vortex State in Confined Ferroelectric Heterostructures

Shang-Lin Hsu, Margaret R. McCarter, Cheng Dai, Zijian Hong, Long-Qing Chen, Christopher T. Nelson, Lane W. Martin, and Ramamoorthy Ramesh*

The manipulation of charge and lattice degrees of freedom in atomically precise, low-dimensional ferroelectric superlattices can lead to exotic polar structures, such as a vortex state. The role of interfaces in the evolution of the vortex state in these superlattices (and the associated electrostatic and elastic boundary conditions they produce) has remained unclear. Here, the toroidal state, arranged in arrays of alternating clockwise/counterclockwise polar vortices, in a confined SrTiO$_3$/PbTiO$_3$/SrTiO$_3$ trilayer is investigated. By utilizing a combination of transmission electron microscopy, synchrotron-based X-ray diffraction, and phase-field modeling, the phase transition as a function of layer thickness (number of unit cells) demonstrates how the vortex state emerges from the ferroelectric state by varying the thickness of the confined PbTiO$_3$ layer. Intriguingly, the vortex state arises at head-to-head domain boundaries in ferroelectric a_1/a_2 twin structures. In turn, by varying the total number of PbTiO$_3$ layers (moving from trilayer to superlattices), it is possible to manipulate the long-range interactions among multiple confined PbTiO$_3$ layers to stabilize the vortex state. This work provides a new understanding of how the different energies work together to produce this exciting new state of matter and can contribute to the design of novel states and potential memory applications.

Emergent phenomena in low-dimensional ferroic materials with functional properties offer exciting opportunities to design and facilitate the miniaturization of future electronic devices.[1–3] The complex interplay of spin, lattice, orbital, and charge degrees of freedom in ferroic systems can result in nontrivial topological textures such as vortices,[4,5] skyrmions,[6] and domain walls[7–9] whose phase transitions and unique properties are intriguing for both fundamental scientific studies and potential applications. For example, magnetic topologies have been well studied theoretically and observed experimentally,[10,11] and routes to control them for spintronic applications, have been demonstrated.[1] Polar structures analogous to these topological magnetic systems have been predicted—such as in ferroelectric nanodots in which spontaneous toroidal moments form[12]—and have led to various theoretical predictions and experiments on low-dimensional ferroelectrics[13–15] due to the effects of constrained dimensionality. The underlying mechanism for the formation and phase transitions of ferroelectric topologies, however, has not been systematically studied. For example, in PbTiO$_3$/SrTiO$_3$ superlattices, the thickness of the layers can drive a complex evolution of the depolarization field. This, coupled with the right substrate strain conditions, can generate dramatically different phenomena, such as improper ferroelectricity for extremely thin PbTiO$_3$/SrTiO$_3$ superlattices[16] and flux-closure domains for thick PbTiO$_3$/SrTiO$_3$ superlattices,[17] and offers a possible route to stabilize polar topological structures.

Dr. S.-L. Hsu, Prof. L. W. Martin, Prof. R. Ramesh
Department of Materials Science and Engineering
University of California
Berkeley, CA 94720, USA
E-mail: rramesh@berkeley.edu

Dr. S.-L. Hsu
The National Center for Electron Microscopy
Molecular Foundry
Lawrence Berkeley National Laboratory
Berkeley, CA 94720, USA

M. R. McCarter, Prof. R. Ramesh
Department of Physics
University of California
Berkeley, CA 94720, USA

C. Dai, Prof. L.-Q. Chen
Department of Materials Science and Engineering
Pennsylvania State University
State College, PA 16802, USA

Dr. Z. Hong
Department of Mechanical Engineering
Carnegie Mellon University
Pittsburgh, PA 15213, USA

Dr. C. T. Nelson
Materials Science & Technology Division
Oak Ridge National Laboratory
Oak Ridge, TN 37831, USA

Prof. L. W. Martin, Prof. R. Ramesh
Materials Science Division
Lawrence Berkeley National Laboratory
Berkeley, CA 94720, USA

Notably, the understanding of toroidal phase stability is crucial for the design of novel states such as ferroelectric skyrmion-like textures.

Recent work has demonstrated the possibility of creating toroidal polarization structures or vortices in $PbTiO_3$/$SrTiO_3$ superlattices with careful control over the superlattice layers at intermediate thicknesses of $PbTiO_3$.[18] The vortex state emerges as a direct consequence of the interplay between the electrostatic and elastic energies, allowing structures with nonuniform polarization textures to form.[19] These $PbTiO_3$/ $SrTiO_3$ superlattices also exhibit emergent chirality due to the formation of chiral arrays of polar vortices.[20] Prior work in this regard has focused on relatively thick (100 nm, approximately eight layer repeats) superlattices, thus keeping the effective macroscopic strain constant. However, several questions have emerged from these observations. First, how does the toroidal state emerge from the ferroelectric state? Second, is the formation of the toroidal state a consequence of long-range interactions among multiple $PbTiO_3$ layers, or are the interactions local to the neighboring layers?

To answer these questions, we reduce the complexity of the superlattice to one of its simplest forms and probe the evolution of polar structures in $(SrTiO_3)_n$/$(PbTiO_3)_n$/$(SrTiO_3)_n$ trilayer heterostructures, wherein the saturation polarization of $PbTiO_3$ in the trilayer heterostructures increases with the $PbTiO_3$ thickness (Figure S1, Supporting Information)

and we focus on intermediate thicknesses of the layers (i.e., n = 12–20 unit cells). We utilize the depolarization effect at the interfaces of $PbTiO_3$ and $SrTiO_3$ and also introduce ≈1% tensile strain from the $DyScO_3$ substrate to manipulate the polar structure in the confined $PbTiO_3$ layer. The trilayer heterostructures on top of the $SrRuO_3$-buffered $DyScO_3$ $(110)_o$ substrates, where o indicates orthorhombic indices, are grown by reflection high-energy electron diffraction-assisted pulsed-laser deposition (Experimental Section). Using a combination of diffraction-contrast, dark-field transmission electron microscopy (DF-TEM) imaging, atomic-scale scanning transmission electron microscopy (STEM) imaging, synchrotron-based reciprocal space mapping, and phase-field modeling, we investigate how and why the toroidal vortex state emerges from the ferroelectric state as the boundary conditions are systematically varied.

To trace the emergence of a vortex state, symmetric $(SrTiO_3)_n$/$(PbTiO_3)_n$/$(SrTiO_3)_n$ (n = 12) trilayer heterostructures were characterized by atomic-resolution STEM imaging in cross-section (**Figure 1**a) (Experimental section). Due to the Z-contrast sensitivity of STEM imaging, the image contrast shows intensity differences between $PbTiO_3$ and $SrTiO_3$ layers (low magnification, Figure S2a, Supporting Information). The microstructure confirms sharp and coherent interfaces with uniform layers, providing a nearly pristine environment in which the polarization can evolve to the vortex state. To determine the polarization configuration with STEM imaging, we
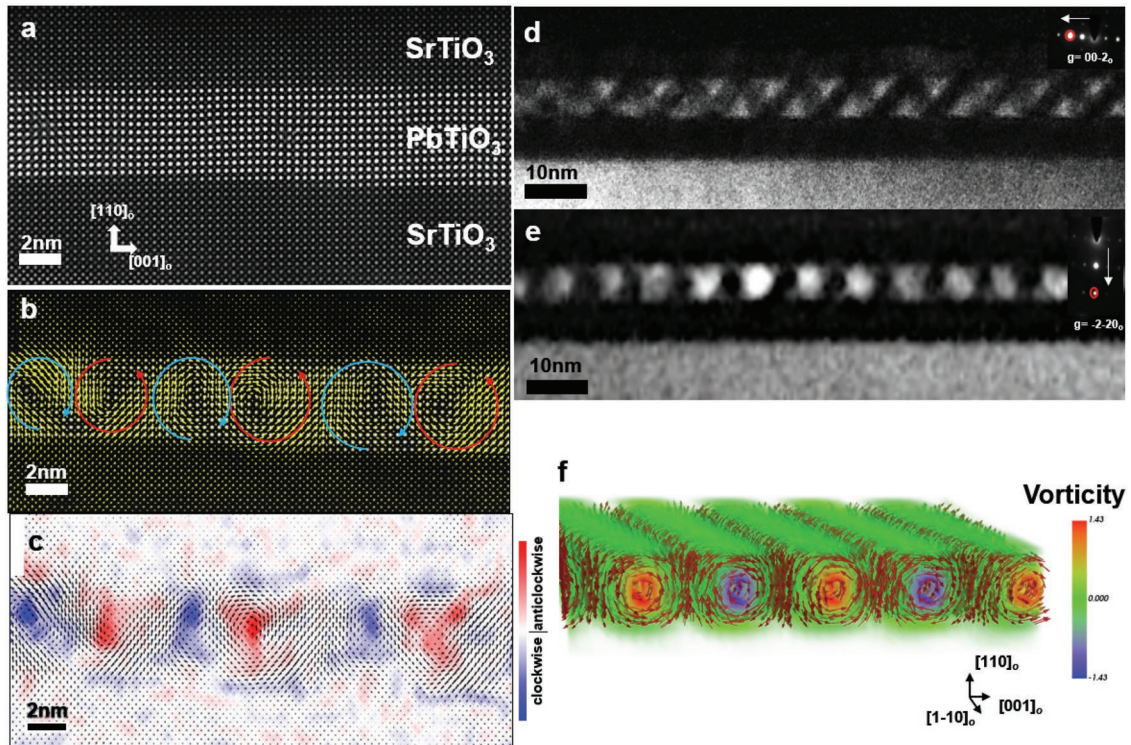

Figure 1. The emergence of polar vortex state in a confined $PbTiO_3$ complex oxide heterostructure. a) High-magnification atomic-resolution HAADF STEM imaging of the trilayer system, $(SrTiO_3)_n$/$(PbTiO_3)_n$/$(SrTiO_3)_n$, in the cross-sectional view (n = 12). b) Atomic polar displacement mapping from region (a) revealing the polarization distribution in $PbTiO_3$ and $SrTiO_3$ layers. The vortex state exists in a single $PbTiO_3$ layer confined between two $SrTiO_3$ layers. c) The curl ($\vec{\nabla} \times \vec{p}$) of the polar displacement vector field to describe vorticity, which indicates alternate blue/red regions representing CW/CCW vortices. d,e) Low-magnification enlarged diffraction contrast DF-TEM imaging in two-beam conditions using $[00\bar{2}]_o$ and $[\bar{2}\bar{2}0]_o$ g-vectors, respectively, which demonstrates the periodic array of modulations revealed only in the $PbTiO_3$ layer. f) Vortex stripes in 3D vector mapping with vorticity predicted by phase-field modeling.

measured the local noncentrosymmetry of the atomic columns between the *A*- and *B*-site sublattices in the ABO_3 lattice to determine the polar structure; this is extracted using a displacement vector-mapping algorithm applied to the cross-sectional atomic resolution STEM images.[13] As a result, the continuous rotation of alternating clockwise (CW) (blue arrows) and counterclockwise (CCW) (red arrows) polar vortices is revealed in the PbTiO$_3$ layer (Figure 1b), as opposed to ferroelectric a_1/a_2 domains observed for short period PbTiO$_3$/SrTiO$_3$ superlattices[21] and flux-closure domains observed for long period PbTiO$_3$/SrTiO$_3$ superlattices.[17] Furthermore, we confirmed the CW (blue areas)/CCW (red areas) vorticity of the vortex state by calculating the curl of the polarization ($\nabla \times p$), which is nonzero in the PbTiO$_3$ layer and zero in the SrTiO$_3$ layers (Figure 1c). Two-beam imaging conditions in DF-TEM (Experimental section) reveal long-range ordering only in the PbTiO$_3$ layer, which indicates a periodic in-plane triangular array when imaged with the $[002]_o$ g-vector and an out-of-plane rectangular array when imaged with the $[\overline{2}20]_o$ g-vector (Figure 1d,e, respectively). These modulations are the critical components of polar vortices, and they correspond to the periodic array of polarization modulations observed in both directions of the atomic-scale STEM polarization analysis of the trilayer system (Figure S2b,c, Supporting Information). 3D polar vector maps from phase-field modeling (Figure 1f) also reveal an equivalent structure with similar stripe-like arrays of CW/CCW vortices laying along the in-plane $[110]_o$ direction in the PbTiO$_3$ layer. The vortex state is found to be stabilized by different contributions from Landau, elastic, electrostatic, and gradient energies (Experimental section). Hence, it can be concluded that even in a single confined PbTiO$_3$ layer, long-range ordering of polar vortices is observed akin to those in superlattices,[18] and such trilayer heterostructures provide a simple model system with which we can deeply probe the emergence of this vortex state.

To better assess how the vortex state emerges from the ferroelectric state, we varied the thickness of the layers in the $(SrTiO_3)_n/(PbTiO_3)_n/(SrTiO_3)_n$ trilayer heterostructures (n = 12, 16, 20). We applied diffraction contrast DF-TEM imaging of a plan view sample using the $[002]_o$ g-vector along with synchrotron-based reciprocal space maps (RSMs) to understand the polarization distribution and phase evolution as a function of layer thickness. For a n = 12 trilayer (**Figure 2**a), the overall light/dark diffraction contrast on the left/right side of the figure indicates the reversal of net polarization along the $[002]_o$ g-vector direction. Inside these broad light and dark regions, the periodic diffraction contrast reveals traditional ferroelectric a_1/a_2 twin domain structures with 45° domain walls and ≈10 nm domain widths, which arises due to the strong depolarization effect driving the polarization into the plane of the film.[21] RSMs of the same heterostructure reveal the absence of ordering in scans about the out-of-plane 220_o-diffraction condition and the presence of ordering in the 45° section of the scan about the off-axis 400_o-diffraction condition (Figure 2g and Figure S3a, Supporting Information). The result supports the idea that the system contains ferroelectric 45° twin domains with ≈10 nm domain width. The experimental results are further supported by the phase-field models, which also reveal twin structures (Figure 2d).

When the layer thickness of the trilayer heterostructures is increased to n = 16 (Figure 2b), most of the ferroelectric a_1/a_2 domains transform to periodic ≈10 nm stripes, now aligned along the $[1\overline{1}0]_o$. This corresponds to the same size and direction of the vortex state probed in the cross-sectional STEM (Figure 1b). The vortex stripes mainly lie along the $[1\overline{1}0]_o$. This is due to the in-plane anisotropy of the DyScO$_3$ substrate,[22] which determines the preferred orientation of the vortex formation. Antiphase boundaries (APBs) between vortex regions can be observed where CW and CCW rotations meet to form an axial domain wall with remaining short segments of ferroelectric a_1/a_2 domains (Figure 2b). RSMs about the on-axis 220_o- and off-axis 400_o-diffraction conditions demonstrate periodic satellites consistent with the presence of both the vortex state and ferroelectric a_1/a_2 domains. The vector mapping done by phase-field modeling predicts CW/CCW rotation of vortex states with APBs as viewed from the top of the trilayer heterostructure (Figure 2e). We conclude that the n = 16 trilayer heterostructures are a mixed-phase system with APBs (Figure 2h and Figure S3b, Supporting Information).

Upon increasing the thickness of the trilayer heterostructure to n = 20 (Figure 2c), most *a*-domains transform into periodic CW/CCW vortex stripes inside these broad light and dark regions, which dominate the entire trilayer system. In the RSMs, the increasing intensity of on-axis 220_o-diffraction satellite peaks indicates that the more stable vortex state is the primary state (Figure 2i). The decreasing intensity of ordering for the off-axis 400_o-diffraction represents the low fraction of ferroelectric a_1/a_2 domains suggesting that the vortex state becomes more stable (Figure S3c, Supporting Information). These structural results are supported by phase-field modeling (Figure 2f). The wide/narrow stripes represent the CW/CCW rotation of vortices due to the asymmetric arrangement between two rotations of the vortex. Hence, the phase evolution demonstrates how the vortex state evolves from the ferroelectric state through the mixed-phase system to the single-phase system.

Given that the evolution from the ferroelectric state to the vortex state manifests as a function of layer thickness, the origin of how the vortex state emerges from the ferroelectric state is intriguing. To explore this metastable vortex state, we studied plan-view diffraction contrast DF-TEM for an n = 12 trilayer, particularly at the boundaries of the ferroelectric domains. The large scale of light/dark diffraction contrast represents the net reversal of polarization in the $[002]_o$ g-vector direction (**Figure 3**a). In this trilayer system, there are four types of boundaries that form to minimize electrostatic energy and remain charge neutral. This boundary between the two a_1/a_2 domains is formed by two sets of head-to-tail domains (the white and green pair of arrows, Figure 3b). At the boundary, 180° domain walls occur in the light stripes (white arrows), resulting in a 90° rotation of the net polarization (red arrows). In turn, this boundary is again formed by two sets of head-to-tail domains (white to green arrows, Figure 3c). Here, 180° domain walls occur in the dark stripes (green arrows). Surprisingly, the head-to-head domains give rise to two types of boundaries (Figure 3d,e). One is the typical in-plane vortex domain (Figure 3d),[23] and the other has the vortex stripes along the $[1\overline{1}0]_o$ (Figure 3e), which are similar to Bloch-point domain walls emerging from two head-to-head spins in 1D
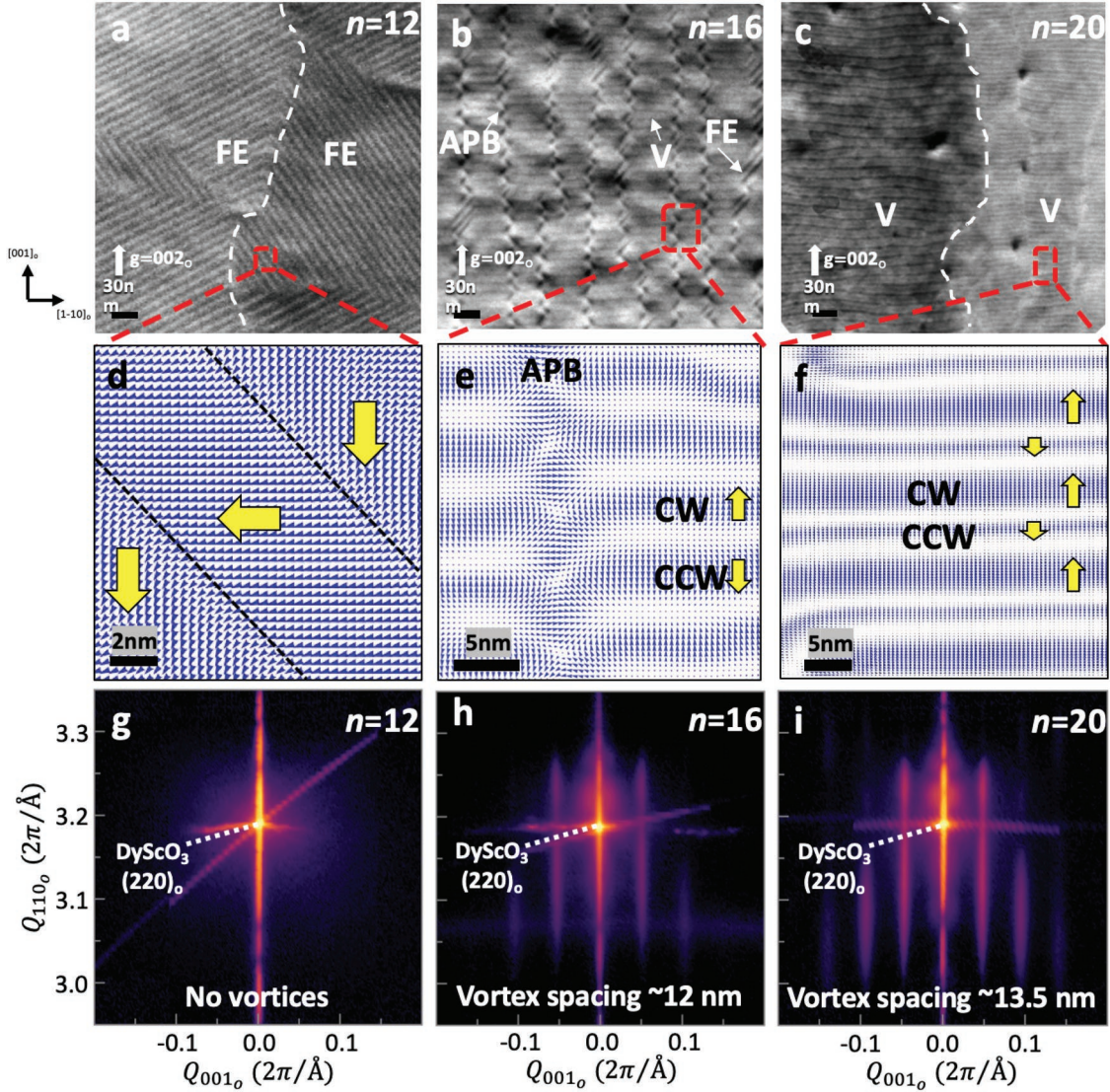
Figure 2. Evolution of the vortex state (V) from the ferroelectric state (FE). Diffraction contrast DF-TEM planar view images in two beam conditions from the PbTiO₃/SrTiO₃ trilayer system, $(SrTiO_3)_n/(PbTiO_3)_n/(SrTiO_3)_m$, exhibit phase evolution: a) $n = 12$, ferroelectric a_1/a_2 twin domains (FE), b) $n = 16$, formation of vortex stripes along $[1\bar{1}0]_o$ with APBs and residual a_1/a_2 twin domains, and c) $n = 20$, vortex state (V). d) Prediction of $n = 12$ by phase-field modeling suggesting ferroelectric state a_1/a_2 twin domains, e) prediction of $n = 16$ suggesting CW/CCW rotation of vortex state and APBs, and f) prediction of $n = 20$ suggesting CW/CCW rotation of vortex state. g–i) The out-of-plane RSM about the $(220)_o$ diffraction condition reveals: g) $n = 12$, no vortex state, h) $n = 16$, formation of vortex state, i) $n = 20$, vortex state.

magnetic nanostripes.[24,25] The polarization distribution at the boundary transforms from the 2D a_1/a_2 state to the 3D vortex state, which allows a decrease of the electrostatic energy and prevents charged domain walls. Vector mapping extracted from the phase-field modeling (Figure 3f) demonstrates that this metastable state is the beginning of the vortex stripes (orange arrow pointing along $[001]_o$ indicating the lateral polarization component of the vortex) along the $[1\bar{1}0]_o$ between two head-to-head domains. Hence, the vortex state emerges between head-to-head ferroelectric a_1/a_2 domains to help minimize electrostatic energy, and then the entire vortex stripes gradually form as a function of layer thickness in the trilayer system.

To further clarify the effect of long-range interactions among multiple PbTiO₃ layers on the formation of the toroidal state,

we investigated the polarization distribution while varying the number of confined PbTiO₃ layers from one to seven (that is, changing from trilayer to superlattice heterostructures). Notably, the ferroelectric a_1/a_2 twin domains were chosen as a starting point for the trilayer ($n = 12$) so as to explore the underlying mechanism of vortex formation when increasing the number of confined PbTiO₃ layers. The low magnification, dark-field TEM images taken with the $[002]_o$ g-vector (**Figure 4**a–d) exhibit mostly bulky, irregular stripes with nonuniform light/dark diffraction contrast, which indicates the reversal of net polarization pointing along $\pm[002]_o$. To gain more insight into this phenomenon, high-magnification images of the stripes were used to explore the local phase distribution (Figure 4e–h). Under the nonuniform light/dark diffraction contrast (Figure 4a),
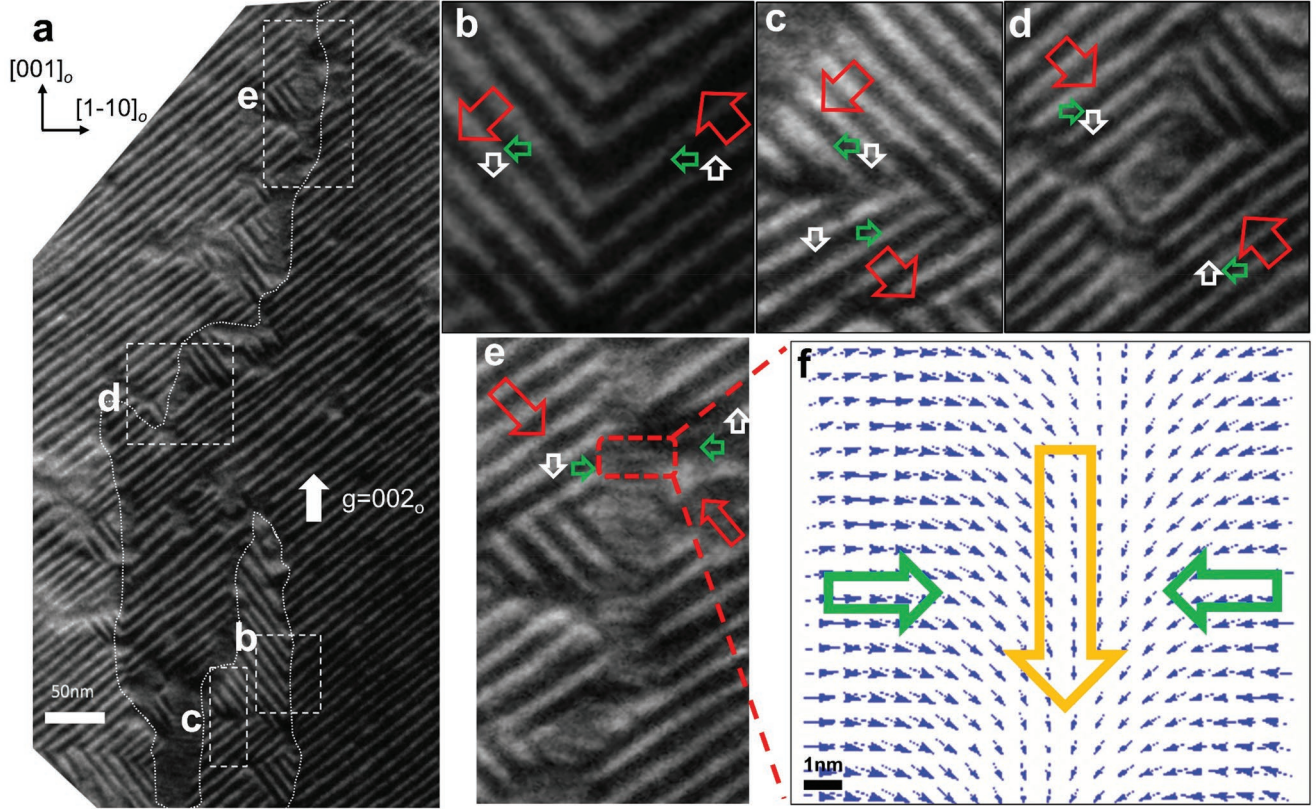
Figure 3. Origins of the vortex state from the boundaries of the FE state ($n = 12$) by diffraction contrast DF-TEM in two beam conditions; a) ferroelectric a_1/a_2 twin domains with four types of boundaries; b,c) Head-to-tail boundary; d) In-plane vortex domain; e) Vortex stripes between head-to-head domains; f) Calculation of the metastable vortex state between head-to-head domains by phase-field modeling.

ferroelectric a_1/a_2 twin domains exist as the primary state (Figure 4e). For three confined PbTiO$_3$ layers (Figure 4b), the nonuniform light/dark diffraction contrast becomes more striped (regular). This implies that the arrangement of polarization distribution is affected by the presence of multiple PbTiO$_3$ layers. At this stacking condition, the ferroelectric a_1/a_2 twin domains are still the primary state (Figure 4f).

When the number of confined PbTiO$_3$ layers increases to five (Figure 4c), the light/dark diffraction contrast changes to ordered stripes, and this implies the enhancement of the alignment of polar structures and phase separation. Remarkably, between these ordered stripes, the local microstructures demonstrate the emergence of vortex stripes along $[1\bar{1}0]_o$ adjacent to the ferroelectric a_1/a_2 twin domains (Figure 4g). This suggests that long-range interactions among multiple PbTiO$_3$ layers can modulate the polarization distribution and can stabilize the vortex state. Finally, the light/dark diffraction contrast indicates the straight, ordered, and continuous stripes in the superlattices with seven confined PbTiO$_3$ layers (Figure 4d). The additional PbTiO$_3$ stacking layers stabilize the phase coexistence of the vortex state and ferroelectric state[19] (Figure 4h). Hence, the phase evolution as a function of PbTiO$_3$ layers demonstrates not only the polarization rearrangement, but also another route to create the vortex state, and this indicates that long-range interactions among multiple PbTiO$_3$ layers play an essential role to influence the vortex stability.

We now capture the phase evolution and the competition between the uniform polar state and the vortex state through a comprehensive 3-D phase diagram obtained by phase-field modeling. **Figure 5**a shows the thermodynamically stable phases with respect to both layer thickness and the number of PbTiO$_3$/SrTiO$_3$ bilayers, which highlights the important role of the total film thickness in forming the vortex phase. The in-plane polarized a_1/a_2 phase is stable at any film thickness when the thickness is under 9 unit cells, indicating that, for such thicknesses of the PTO layer, the depoling field dominates the total energetics of the system, thus favoring the formation of in-plane ferroelectric domains. On the other hand, when the thickness is above 14 unit cells, the vortex phase is the thermodynamic ground state. For layer thickness in between, there is a competition between the in-plane polar state and the vortex state; under such circumstances, the total film thickness plays an important role in deciding which phase is stable. A transition to a mixture of a_1/a_2 and vortex phases driven by film thickness is thus one of the key conclusions from this phase competition. This is captured for the case of a 11 unit cell layer thickness shown in the dashed rectangle, for which the in plane a_1/a_2 twin domains transform to the mixed phase when the number of (PbTiO$_3$/SrTiO$_3$) bilayers is increased from 1 to 7. The vortex state is obtained in thicker films in good agreement with the experimental observations.

One can also compare the total energy density and the two main components, namely the elastic and electric energies for
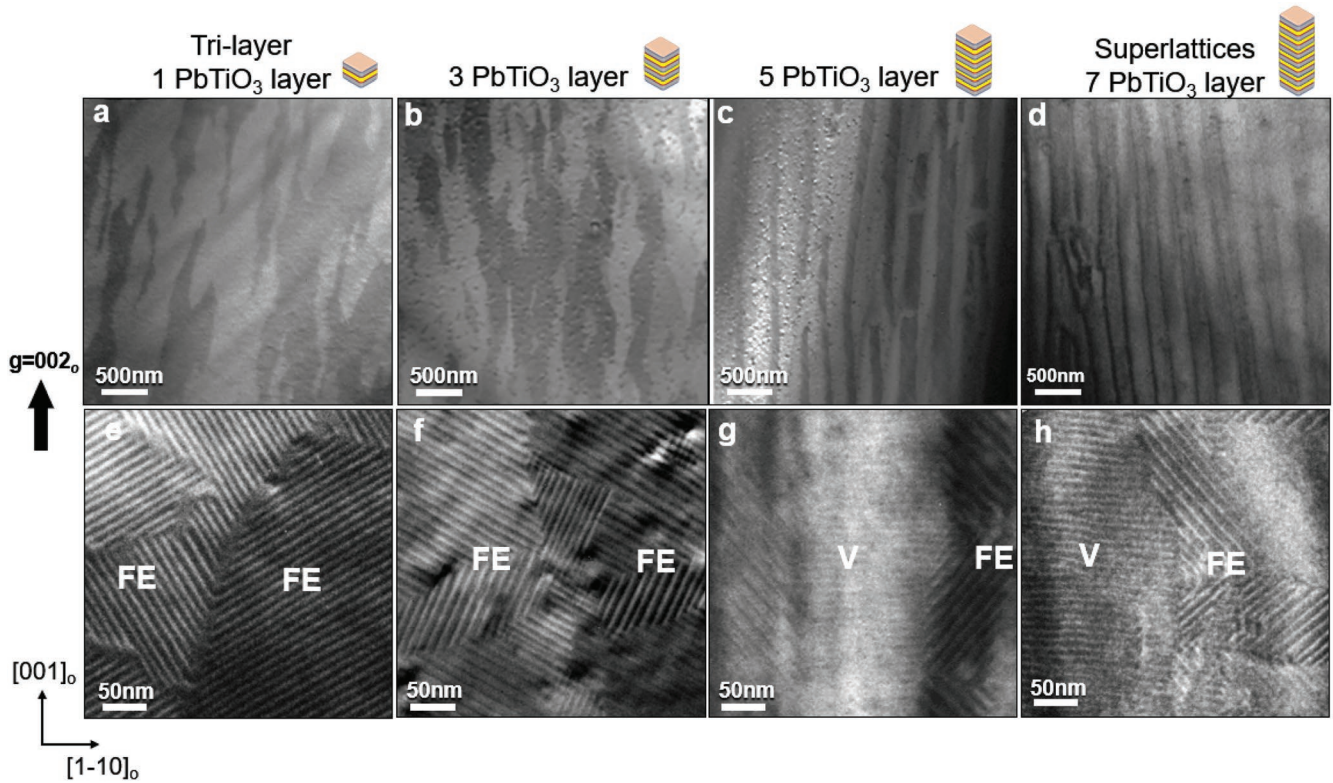
Figure 4. Formation of the vortex state from PbTiO$_3$/SrTiO$_3$ trilayer ($n = 12$) to PbTiO$_3$/SrTiO$_3$ superlattices ($n = 12$) observed by diffraction contrast DF-TEM at low and high magnifications: a–d) the low-magnification images represent 1, 3, 5, and 7 confined PbTiO$_3$ layers; e–h) the high-magnification images ranging from the previous trilayer to the superlattice low-magnification regions exhibit the evolution from full FE states to phase coexistence of FE and V states.
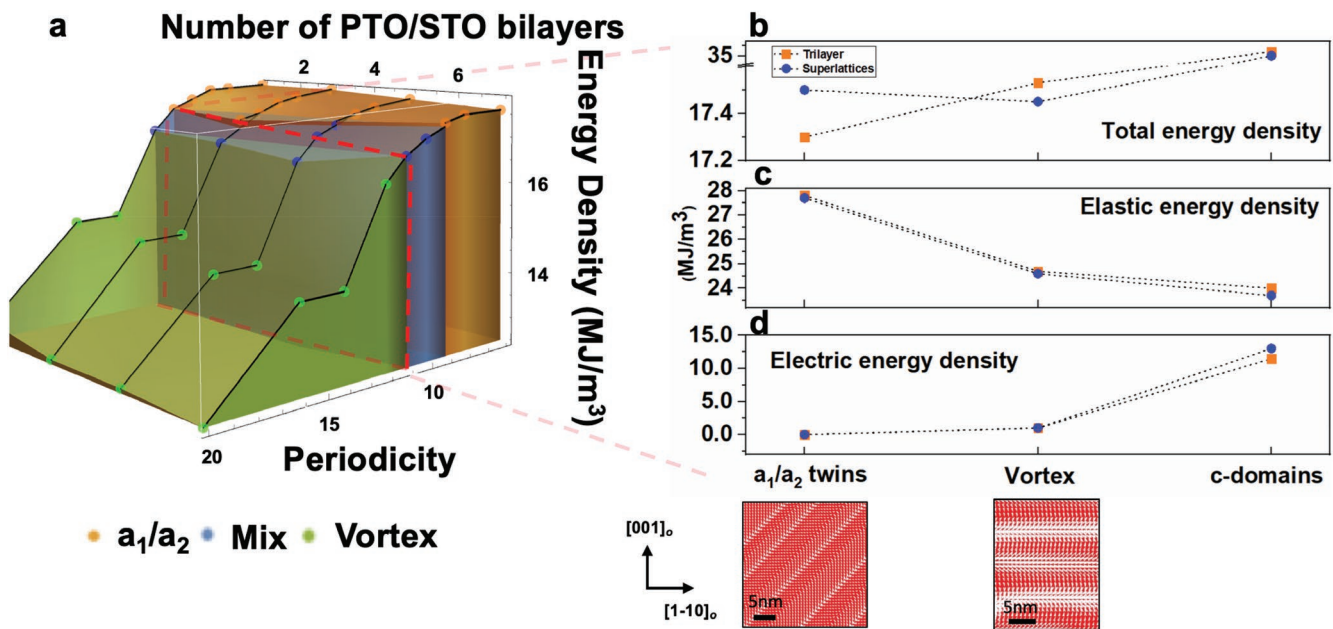

Figure 5. Film-thickness dependent polar structure transition for the PbTiO$_3$/SrTiO$_3$ trilayer to PbTiO$_3$/SrTiO$_3$ superlattices calculated by phase-field simulation; a) 3D phase diagram. Energy comparison between a_1/a_2 twin, vortex, and c-domains taken through the slice shown by the dashed rectangle: b) total energy density; c) elastic energy density; d) electric energy density.

the two phases as a function of the number of bilayer thickness, Figure 5b, specifically for the 11-unit cell trilayer and superlattices. For a trilayer, the lowest energy state clearly corresponds to the a_1/a_2 in-plane polarized state (orange squares). In contrast, for the superlattice, the difference in total energy between the a_1/a_2 and the vortex state is not significant (blue circles and orange squares) indicating that a mixed phase coexistence is likely. The energy density of c-domains as the transient state is shown for comparison and clearly this is not favored. The total energy density decrease is mainly attributed to the decrease of the average elastic energy density, which is understood since the vortex state has a higher ratio of elastically favorable out-of-plane polarization (Figure 5c). The electric energy density increases slightly due to the out-of-plane polarization of the vortex state (Figure 5d). From an energetic point of view, the film thickness-driven phase transition (while keeping the layer thickness constant) is a result of the competition between the individual energies—elastic, electric, Landau, and gradient. The increasing layer stacking leads to a decrease of elastic energy, which counterbalances the energy penalty of a higher gradient energy and a higher electric energy arising from the complex polar texture. Hence, it is revealed that the formation of the vortex state can be triggered by not only layer thickness, but also by increasing the number of confined $PbTiO_3$ layers, showing the importance of long-range elastic interactions among the $PbTiO_3$ layers.

To summarize, our investigations have demonstrated that the vortex state can be stabilized in a single confined $PbTiO_3$ layer, which acts as a simple model system to study the polarization distribution. The polarization distribution demonstrates the phase evolution from a ferroelectric state to a vortex state by utilizing the thickness dependence of the trilayer heterostructures. Notably, the origin of the vortex state is introduced by head-to-head domains between ferroelectric a_1/a_2 domains to minimize electrostatic energy during the beginning of the phase evolution. Ultimately, tipping the energy balance of the system can be another route to excite the vortex state by using elastic energy from the long-range interactions in the $PbTiO_3/SrTiO_3$ system. These studies should contribute to the further understanding of novel polarization topologies and provide possible routes to design polarization topologies that enable the development of high-density memory devices.

Experimental Section

Sample Growth: The $(PbTiO_3)_n/(SrTiO_3)_n$ trilayer heterostructures (n = 12, 16, 20) were synthesized by reflection high-energy electron diffraction-assisted pulsed laser deposition with a KrF excimer laser. A buffer layer of ≈5 nm of $SrRuO_3$ was deposited on the $DyScO_3$ (110)$_o$ substrates at a temperature of 700 °C and oxygen pressure of 50 mTorr. For trilayer structures, the bottom $SrTiO_3$ layer was deposited at the same conditions as $SrRuO_3$. Subsequent layers of $PbTiO_3$ and $SrTiO_3$ were deposited at 620 °C and 100 mTorr oxygen pressure. For all materials, the laser fluence was ≈1.5 J cm^{-2}, and the laser repetition rate was 10 Hz. After the deposition, heterostructures were cooled in 50 Torr of oxygen to room temperature. The films were grown from a single crystalline $SrTiO_3$ target and polycrystalline $SrRuO_3$ and $Pb_{1.2}TiO_3$ targets.

Conventional and Scanning Transmission Electron Microscopy: Cross-sectional and planar-view TEM samples were prepared by mechanical polishing on an Allied High Tech Multiprep at 0.5° wedge polish followed by low-angle argon-ion milling at 4 keV and cleaning at 200 eV. The characterization of microscopic structures was mainly performed by the diffraction-contrast TEM on FEI TitanX 60-300 microscope operated at 300 kV, and the STEM imaging on spherical aberration (Cs) corrected FEI Titan 80-300 operated at 300 kV giving a point-to-point resolution of 50 pm at the National Center for Electron Microscopy, Lawrence Berkeley National Laboratory. Diffraction contrast imaging is an efficient tool to determine the polarization directions of local domain structures by using the failure of Friedel's law in electron diffraction on ferroelectric materials lacking a symmetry center. By tilting the TEM sample away from the zone axis, two-beam conditions are formed with the diffracted beam along the optical axis. The selected crystallographic plane, corresponding to the [002]$_o$ g-vector, was imaged to acquire the polarization directions through contrast. The local polarization distribution was demonstrated by atomic resolution STEM (Z-contrast) imaging with atomic displacement mapping described in previous work.[18,19]

Structural Characterization—Synchrotron-Based X-Ray Diffraction: Synchrotron-based X-ray diffraction studies were performed at beamline 33-BM-C at the Advanced Photon Source, Argonne National Laboratory. 3D reciprocal space maps (RSMs) were acquired using the Huber 4-circle diffractometer and the PILATUS 100K pixel detector. The high flux of X-rays available at the synchrotron coupled with 3D RSMs allowed us to measure satellite diffraction peaks that arose from the ordering of both the in- and out-of-plane polarization components in the heterostructures. Slices from 3D RSMs along the 001$_o$- and $\bar{1}11_o$-directions showed the presence or absence of satellite peaks due to periodic polar vortices or ferroelectric domains, respectively.

Phase-Field Simulations: In the phase-field modeling of the $PbTiO_3/SrTiO_3$ multilayer system, the evolution of the polarization was obtained by solving the time-dependent Ginzburg–Landau (TDGL) equations

$$\frac{\partial P_i(\vec{r},t)}{\partial t} = -L\frac{\delta F}{\delta P_i(\vec{r},t)} (i = 1, 2, 3) \tag{1}$$

where L, r, and t denote the kinetic coefficient, spatial position vectors, and time, respectively. The contributions to the total free energy F include the Landau bulk energy, elastic energy, electric (electrostatic) energy, and gradient energy, i.e.,

$$F = \int \left(f_{Landau} + f_{Elastic} + f_{Electric} + f_{Gradient} \right) dV \tag{2}$$

The expression for each energy density can be found in the literature.[26–28] Due to the inhomogeneity of elastic constants in the $[(SrTiO_3)_m/(PbTiO_3)_m]_n$ multilayer system, a spectral iterative perturbation method was employed to solve the mechanical equilibrium equation to obtain the stress field.[29] The pseudocubic lattice constants for $PbTiO_3$ and $SrTiO_3$ were taken as 3.9547 and 3.905 Å, respectively,[30] while the anisotropic in plane lattice constants for the substrate $DyScO_3$ were taken from the literature to calculate the misfit strain.[31] Material constants for $PbTiO_3$ and $SrTiO_3$ used in the simulations are found from the literature, and these include the Landau potentials, elastic constants, electrostrictive coefficients, background dielectric constants, and gradient energy coefficients.[27,30,32–35]

The 3D phase-field simulation of the $[(SrTiO_3)_m/(PbTiO_3)_m]_n$ multilayer system is done using discrete grids of (100Δx) × (100Δy) × (350Δz) with $\Delta x = \Delta y = \Delta z = 0.4$ nm, where Δx, Δy, and Δz are in real space. The thickness of the substrate, film, and air are 30Δz, ((2n + 1) × (m − 1))Δz, and (321-(2n + 1) × m)Δz, respectively, where n is the number of confined $PbTiO_3$ layers. In the film, alternating (m − 1) grids of $PbTiO_3$ layers and (m − 1) grids of $SrTiO_3$ layers with one transition layer in between were incorporated to simulate the multilayer system. The thickness of $PbTiO_3$ and $SrTiO_3$ layers effectively describes the experimental observation. Periodic boundary conditions were assumed in both the x and y directions and a superposition method was used along the z-direction.[27] Random noise with a magnitude of 0.01 μC cm^2 was used as the initial setup to simulate the thermal fluctuation during the annealing process.

Acknowledgements

[1] A. Fert, V. Cros, J. Sampaio, *Nat. Nanotechnol.* **2013**, *8*, 152.
[2] G. Catalan, J. Seidel, R. Ramesh, J. F. Scott, *Rev. Mod. Phys.* **2012**, *84*, 119.
[3] A. Soumyanarayanan, N. Reyren, A. Fert, C. Panagopoulos, *Nature* **2016**, *539*, 509.
[4] M. Y. Im, P. Fischer, K. Yamada, T. Sato, S. Kasai, Y. Nakatani, T. Ono, *Nat. Commun.* **2012**, *3*, 983.
[5] A. Ruotolo, V. Cros, B. Georges, A. Dussaux, J. Grollier, C. Deranlot, R. Guillemet, K. Bouzehouane, S. Fusil, A. Fert, *Nat. Nanotechnol.* **2009**, *4*, 528.
[6] R. Wiesendanger, *Nat. Rev. Mater.* **2016**, *1*, 16044.
[7] H. Béa, P. Paruch, *Nat. Mater.* **2009**, *8*, 168.
[8] P. Schoenherr, J. Müller, L. Köhler, A. Rosch, N. Kanazawa, Y. Tokura, M. Garst, D. Meier, *Nat. Phys.* **2018**, *14*, 465.
[9] S. Emori, U. Bauer, S. M. Ahn, E. Martinez, G. S. D. Beach, *Nat. Mater.* **2013**, *12*, 611.
[10] A. Wachowiak, J. Wiebe, M. Bode, O. Pietzsch, *Science* **2002**, *298*, 577.
[11] T. Shinjo, T. Okuno, R. Hassdorf, K. Shigeto, T. Ono, *Science* **2000**, *289*, 930.
[12] I. I. Naumov, L. Bellaiche, H. Fu, *Nature* **2004**, *432*, 737.
[13] C. T. Nelson, B. Winchester, Y. Zhang, S. J. Kim, A. Melville, C. Adamo, C. M. Folkman, S. H. Baek, C. B. Eom, D. G. Schlom, L. Q. Chen, X. Pan, *Nano Lett.* **2011**, *11*, 828.
[14] C. L. Jia, K. W. Urban, M. Alexe, D. Hesse, I. Vrejoiu, *Science* **2011**, *331*, 1420.
[15] P. Zubko, N. Jecklin, A. Torres-Pardo, P. Aguado-Puente, A. Gloter, C. Lichtensteiger, J. Junquera, O. Stéphan, J. M. Triscone, *Nano Lett.* **2012**, *12*, 2846.
[16] E. Bousquet, M. Dawber, N. Stucki, C. Lichtensteiger, P. Hermet, S. Gariglio, J. M. Triscone, P. Ghosez, *Nature* **2008**, *452*, 732.
[17] Y. L. Tang, Y. L. Zhu, E. A. Eliseev, W. Y. Wang, Y. J. Wang, Y. B. Xu, Z. D. Zhang, S. J. Pennycook, *Science* **2015**, *348*, 1259869.
[18] A. K. Yadav, C. T. Nelson, S. L. Hsu, Z. Hong, J. D. Clarkson, C. M. Schlepütz, A. R. Damodaran, P. Shafer, E. Arenholz, L. R. Dedon, *Nature* **2016**, *530*, 198.
[19] A. R. Damodaran, J. D. Clarkson, Z. Hong, H. Liu, A. K. Yadav, C. T. Nelson, S. L. Hsu, M. R. McCarter, K. D. Park, V. Kravtsov, A. Farhan, Y. Dong, Z. Cai, H. Zhou, P. Aguado-Puente, P. Garcia-Fernandez, J. Iniguez, J. Junquera, A. Scholl, M. B. Raschke, L. Q. Chen, D. D. Fong, R. Ramesh, L. W. Martin, *Nat. Mater.* **2017**, *16*, 1003.
[20] P. Shafer, P. García-Fernández, P. Aguado-Puente, A. R. Damodaran, A. K. Yadav, C. T. Nelson, S.-L. Hsu, J. C. Wojdeł, J. Íñiguez, L. W. Martin, E. Arenholz, J. Junquera, R. Ramesh, *Proc. Natl. Acad. Sci. USA* **2018**, *115*, 915.
[21] Z. Hong, A. R. Damodaran, F. Xue, S. L. Hsu, J. Britson, A. K. Yadav, C. T. Nelson, J. J. Wang, J. F. Scott, L. W. Martin, R. Ramesh, L. Q. Chen, *Nano Lett.* **2017**, *17*, 2246.
[22] M. Janovská, P. Sedlák, H. Seiner, M. Landa, P. Marton, P. Ondrejkovič, J. Hlinka, *J. Phys.: Condens. Matter* **2012**, *24*, 385404.
[23] N. Balke, B. Winchester, W. Ren, Y. H. Chu, A. N. Morozovska, E. A. Eliseev, M. Huijben, R. K. Vasudevan, P. Maksymovych, J. Britson, S. Jesse, I. Kornev, R. Ramesh, L. Bellaiche, L. Q. Chen, S. V. Kalinin, *Nat. Phys.* **2012**, *8*, 81.
[24] S. Da Col, S. Jamet, N. Rougemaille, A. Locatelli, T. O. Mentes, B. S. Burgos, R. Afid, M. Darques, L. Cagnon, J. C. Toussaint, O. Fruchart, *Phys. Rev. B* **2014**, *89*, 180405.
[25] A. Fernández-Pacheco, R. Streubel, O. Fruchart, R. Hertel, P. Fischer, R. P. Cowburn, *Nat. Commun.* **2017**, *8*, 15756.
[26] L. Q. Chen, *J. Am. Ceram. Soc.* **2008**, *91*, 1835.
[27] F. Xue, J. J. Wang, G. Sheng, E. Huang, Y. Cao, H. H. Huang, P. Munroe, R. Mahjoub, Y. L. Li, V. Nagarajan, L. Q. Chen, *Acta Mater.* **2013**, *61*, 2909.
[28] J. J. Wang, X. Q. Ma, Q. Li, J. Britson, L. Q. Chen, *Acta Mater.* **2013**, *61*, 7591.
[29] Y. L. Li, S. Y. Hu, Z. K. Liu, L. Q. Chen, *Acta Mater.* **2002**, *50*, 395.
[30] Y. L. Li, S. Y. Hu, Z. K. Liu, L. Q. Chen, *Appl. Phys. Lett.* **2002**, *81*, 427.
[31] L. Q. Chen, J. Shen, *Comput. Phys. Commun.* **1998**, *108*, 147.
[32] M. J. Haun, E. Furman, S. J. Jang, H. A. McKinstry, L. E. Cross, *J. Appl. Phys.* **1987**, *62*, 3331.
[33] G. Sheng, Y. L. Li, J. X. Zhang, S. Choudhury, Q. X. Jia, V. Gopalan, D. G. Schlom, Z. K. Liu, L. Q. Chen, *Appl. Phys. Lett.* **2010**, *96*, 10.
[34] Z. H. Chen, A. R. Damodaran, R. Xu, S. Lee, L. W. Martin, *Appl. Phys. Lett.* **2014**, *104*, 182908.
[35] R. Uecker, B. Velickov, D. Klimm, R. Bertram, M. Bernhagen, M. Rabe, M. Albrecht, R. Fornari, D. G. Schlom, *J. Cryst. Growth* **2008**, *310*, 2649.